5-5-2018

Development of Tools for a 3D Reconstructed Intracortical Volume Around Microelectrode Arrays

Aparna Nambiar
aparna.nambiar@uconn.edu

Development of Tools for a 3D Reconstructed Intracortical Volume Around Microelectrode Arrays

Aparna Nambiar

B.E., Sri Jayachamarajendra College of Engineering, 2014

A Thesis

Submitted in Partial Fulfillment of the

Requirements for the Degree of Master of Science

at the

University of Connecticut

2018

APPROVAL PAGE

Masters of Science Thesis

Development of Tools for a 3D Reconstructed Intracortical Volume Around Microelectrode Arrays

Presented by

Aparna Nambiar, B.E.

Major Advisor _____
Dr. Martin Han

Associate Advisor _____
Dr. Guoan Zheng

Associate Advisor _____
Dr. Sabato Santaniello

University of Connecticut

2018

ACKNOWLEDGEMENTS

I would like to take this opportunity to express my gratitude to my advisor Dr. Martin Han for giving me this wonderful opportunity to work in this exciting field of neural engineering. His unwavering support and encouragement has helped me grow and develop my skills in scientific research, root cause analysis and scientific presentation. I would also like to thank my associate advisors Dr. Guoan Zheng and Dr. Sabato Santaniello for their scholarly advice, guidance and motivation. I am also grateful to Dr. Nicholas Nolta for his invaluable support and suggestions in completing my thesis. I would also like to thank Haison Duong whose research has been of significant contribution to this project.

I owe a deep sense of gratitude to my parents Suresh Nambiar and Geetha Suresh, my sister Deepika Nambiar, and my brother-in-law Sunoj Nambiar, for being my pillars of support with their unconditional love for me and immense faith in my abilities.

Last but not the least, I would like to thank all my friends, roommates and lab mates for their moral support and goodwill towards me who taught me: “When the going gets tough, the tough get going.”

CONTENTS

ABSTRACT

Extensive research using penetrating electrodes implanted in the central and peripheral nervous systems has been performed for many decades with significant advances made in recent years. While these penetrating devices provide proximity to individual neurons *in-vivo* and perform effectively for several months, they are prone to failure over a year and longer. 2D Histology studies using serial tissue sections have been extremely insightful over the years in identifying and quantifying most of these factors such as astrocytic scar formation, microgliosis, and neuronal death, to name a few, around the implant sites. However, there are significant limitations of 2D histological studies in providing a holistic picture of the problems occurring at the electrode-tissue interface. In this study, we present 3D reconstruction of serial sections to overcome the limitations of 2D histological analysis. We used a cohort of software: XuvStitch™ (XuvTools), AutoAligner™ (Bitplane AG), and Imaris™ (Bitplane AG), and coupled these with MATLAB (The MathWorks, Inc.) programming to correct warping effects and misalignment issues. Once the 3D image volume is reconstructed, we were able to use features of Imaris™ to quantify neuronal densities and astrocytic scar tissue densities around the electrode tips of a hybrid microelectrode array. Additionally, this study also demonstrated advantages of quantifying around different types of microelectrodes of a hybrid array in the same intracortical space eliminating confounding factors such as varying implantation sites, lengths of study, different animals, so on and so forth and thereby, the performance of the microelectrodes can be attributed solely to device material properties and device fabrication process.

CHAPTER 1

INTRODUCTION

Numerous studies have been conducted using electrodes implanted in the central and peripheral nervous systems to stimulate neurons and record neuronal action potentials to treat neurological disorders (Kook, Lee, Lee, Cho, & Lee, 2016). There have been major breakthroughs in the field that have improved quality of life for many patients globally. One of the most prominent ones is the cochlear implant that helps in restoring hearing impairment and resolving vertigo spells and tinnitus due to disorders of the inner ear (Yawn, Hunter, Sweeney, & Bennett, 2015). Another breakthrough is the deep brain stimulation used to treat debilitating motor symptoms of Parkinson's disease as well as psychiatric disorders, by implanting electrodes deep within the brain (Fang & Tolleson, 2017; Holtzheimer & Mayberg, 2011). More recently, silicon-based Blackrock microelectrodes have been FDA-approved for brain-machine interfaces (Downey et al., 2016).

Generally, there are two types of electrodes: non-invasive electrodes and invasive electrodes, each with advantages and disadvantages of their own. While non-invasive electrodes are widely used to record from large populations of neurons

(Electroencephalography (EEG)) at low risk and cost, invasive electrodes are far more superior in signal quality and information density (Waldert, 2016). The latter can penetrate deep into the regions of interest in the brain and detect neuronal activity of even small clusters of neurons (spikes). In particular, penetrating microelectrodes can detect high frequency neuronal single and multi-unit signals which would otherwise be undetected by their non-invasive counter-parts. A recent approval by the FDA for the brain machine interface (BMI) underscored its potential (Collinger et al., 2013).

Despite these advances, chronic implants often cease to record neural spike signals over time (Liu et al., 1999). The implants may start malfunctioning after several months and may ultimately fail to record spike signals although local field potentials persist. This can be attributed to various factors such as foreign body response (FBR), neuronal death, and hardware related issues. FBR is characterized by an acute inflammation which involves macrophages, microglia, astrocytes and blood brain-barrier leakage. A number of histological studies using slice-by-slice analysis have been conducted to characterize these multi-disciplinarian factors in the electrode-tissue interface. In one study carried out for twelve weeks, they correlated single unit recording performances and FBR. Neuronal death around the implant site were also observed (Nolta, Christensen, Crane, Skousen, & Tresco, 2015; Salatino, Ludwig, Kozai, & Purcell, 2017). Other studies, carried out for approximately a year, correlated the amplitude of neuronal action potential and signal-to-noise-ratio with the neuronal cell death and the formation of astrocytic scar tissue formation (Liddelow et al., 2017; McCreery, Cogan, Kane, & Pikov, 2016). These studies showed that the area immediate to the electrode sites have a lower density of healthy neurons and have denser astroglial scar tissue encapsulation which are major factors

responsible for loss of neuronal signal data. These studies quantified their data in the lateral space around the electrodes. Also, they used only one type of electrode, and hence, it is not suitable to generalize these findings to other types of intracortical electrodes.

While 2D histological studies have been used extensively to characterize tissue response around intracortical electrodes for years, they have some major limitations. In most studies, the histological analysis of neural tissue was carried out along the entire length of the electrode, thus not specific to the active, deinsulated exposed tip of the electrode which is where neuronal spikes are picked up. This was especially true if the analysis was done for coronal sections of tissue (Freire et al., 2011; Nelson et al., 2010). This could lead to an inaccurate analysis of the extent of influence of foreign body response on the long-term recording performance of the electrodes. Additionally, in 2D studies, quantification of neural cell bodies is done in the lateral space around the shank and not in the space below the tip of the electrode. This is applicable to tip-based devices such as Microprobe microwires and Blackrock electrodes. Insertion of the microelectrode shank displaces neural tissue but may disrupt those under the tip to a much lesser degree. Hence, some of the healthy neurons in the tissue below the tip contributing to the recording quality of the electrode may go uncounted and this could lead to inaccurate correlation of neuronal density with recording data. Finally chronic tethering forces – both tangential causing displacement in the z-direction and radial causing displacement in the x-y direction (Karumbaiah et al., 2013; Weltman, Yoo, & Meng, 2016), brain tissue micromotion (Gilletti & Muthuswamy, 2006) and tissue response to the electrode could cause the electrode array to get dislocated, changing the position and orientation of the

electrodes within the brain. These changes make 2D distance quantification around the electrode site more challenging and prone to errors.

The structure of the brain is three-dimensional (3D) as is the device. Thus, two-dimensional analysis of these three-dimensional objects is not only lacking, but also can lead to inaccurate conclusions. Therefore, there is a growing interest to analyze and quantify in a 3D volume rather than being limited to a series of tissue slices. Distance quantifications in any direction around the electrode site are possible and more feasible in a 3D spatial arrangement of neural tissue components.

Broadly speaking, the major steps that encompass a 3D reconstruction include: stacking up of confocally scanned physical sections, eliminating imaging artifacts, aligning the sections to form a continuous 3D volume, after which quantification based on intensity or feature can be carried out. Recent advances in 3D rendering and reconstruction software have enabled researchers to reconstruct whole tissue blocks of interest. However, most of these studies are restricted to the visualization of the reconstructed 3D volume and do not attempt to quantify the cellular structures in the tissue volume. One group reconstructed a 3D volume of the inferior colliculus of the midbrain to study the functionalities of an auditory midbrain implant using a 3D reconstruction software called Rhino 3D (Markovitz, Tang, Edge, & Lim, 2012). In another study, they used a custom-built algorithm to automate the 3D reconstruction process of a mammary gland tissue for visualization (Arganda-Carreras, Fernández-González, Muñoz-Barrutia, & Ortiz-De-Solorzano, 2010). In addition, other 3D reconstruction studies centered around correcting the 3D volume artifacts such as planar and non-planar axial distortion (Berlanga et al., 2011; Hanslovsky, Bogovic, & Saalfeld, 2017). Also, most of these techniques cannot be

applied to a wide range of image datasets and are not repeatable. One group attempted to reconstruct 3D cells of neurons in the somatosensory cortex from confocal z-stacks using 2D segmentation technique. They were able to count and correctly identify between 91-94% of the cells (LaTorre, Alonso-Nanclares, Muelas, Peña, & DeFelipe, 2013). Another study investigated the spatial arrangement and morphology of neuroblasts in the lateral striatum using an opensource software called Reconstruct (Luzzati, Fasolo, & Peretto, 2011). Some groups built custom algorithms for detecting neurons from large confocal image stacks and visualizing large canvases 3D canvas of the region of interest within the brain (Peng, Ruan, Long, Simpson, & Myers, 2010; Yayon et al., 2018). TABLE 1 shows a quick comparison of some of the widely used 3D reconstruction software.

TABLE 1. A summary of widely used 3D reconstruction software

3D reconstruction software	Pros	Cons
ImageJ (https://imagej.nih.gov/)	• Free • Open platform • Friendly user interface	• Cannot handle large datasets (2GB limit)
Image-Pro Premier 3D (Media Cybernetics, Inc.)	• Medium priced • Has a wide variety of features for quantification	• Program freezes and works incorrectly for large datasets
Amira-Avizo (Thermo Fisher Scientific.)	• Can handle large datasets • Has a wide variety of features for quantification • Interfacing options	• No alignment module of its own
Rhinoceros 3D (Robert McNeel & Associates.)	• Free • Easy to use	• More suitable for 3D modelling • Lacks features for quantification
Voloom (microDimensions GmbH)	• Good for automatic alignment (data should have good fiducials) • Medium priced	• Difficult to carry out manual alignment for large datasets • Can't zoom in to micron level while aligning • Not many features for quantification
Imaris (Bitplane AG)	• Has a wide variety of features for quantification • Can handle large datasets • Interfacing options with MATLAB and Python for developing custom functionalities	• No alignment module of its own

Some of the challenges faced while attempting to reconstruct a 3D volume are warped tissue sections due to the manual nature of sectioning and gross misalignments when the tissue is mounted on the slide and during the image acquisition process. There will also be certain local shrinkages and expansions due to solvent- and heat-treatment involving staining of the tissues using antibody biomarkers. Examples of misalignments are illustrated in FIGURE 1.

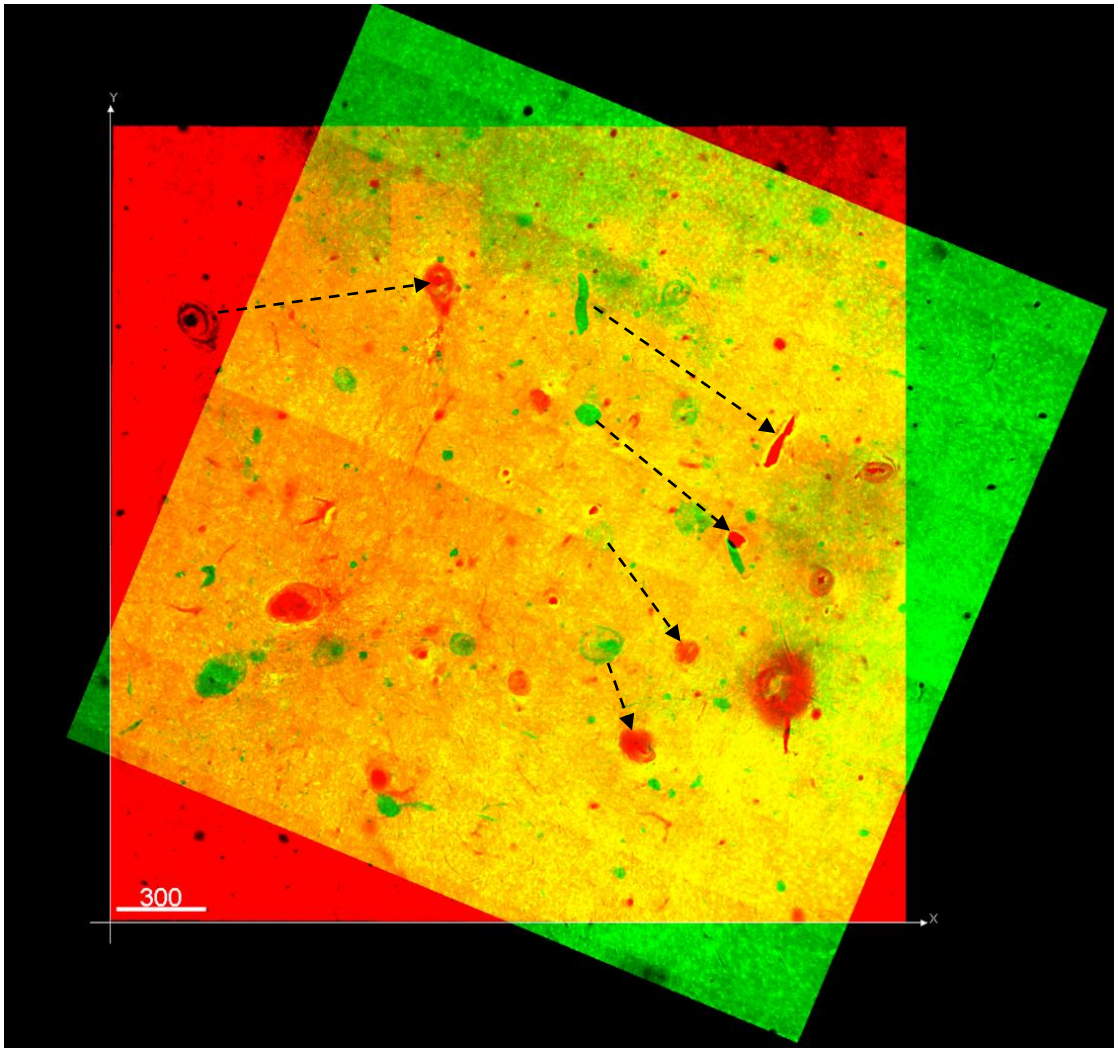

FIGURE 1. An illustration of yet to be aligned consecutive confocally-scanned tissues. The top two images are unaligned images of two consecutive sections. A red slice and a green slice can be seen overlaid on each other to distinctly identify the lack of alignment between the sections. Arrows indicate the fiducials that need to be aligned between the two slices.

In this study, we are presenting a 3D reconstruction workflow of an intracortical tissue volume using stitching software XuvStitch™, 3D image reconstruction software Imaris™, manual alignment software AutoAligner™ and MATLAB programming. Once the 3D volume is built, quantification of neuronal and astrocytic densities is carried out using features of Imaris™ for individual electrodes of the hybrid array. Additionally, this study used a hybrid array with three broad types of electrodes (U.S. Patent Application No. 20130150696A, 2013). The motivation behind using a hybrid array to carry out to study the long-term effects of foreign body response on electrode performance is that we can make fair comparisons of different device performances. Device failures can be attributed to the device material, fabrication processes and not to other external factors like implantation sites, implantation techniques, analysis methods, length of study, different animals etc. To the best of our knowledge, this is the first ever study developing a true 3D image of intracortical tissue around an array of microelectrode sites.

CHAPTER 2

MATERIALS AND METHODS

2.1 Devices and Methods

Microelectrode tips from twenty-two hybrid electrode arrays —mentioned above were implanted in eleven male cats' cerebral cortex. The implantation durations ranged 4 weeks to 58 weeks, providing a variety of chronic behaviors possible in the brain tissues. Each hybrid array (see FIGURE 2.1) consisted of eight 1 mm long Utah intracortical electrodes (Blackrock Microsystems, LLC), four 1.5 mm long silicon substrate probes (NeuroNexus), four short 1 mm long microwires (Microprobes) and four 1.5 mm long microwires (Microprobes). There is at least one active site at the 1 mm-depth for each electrode.

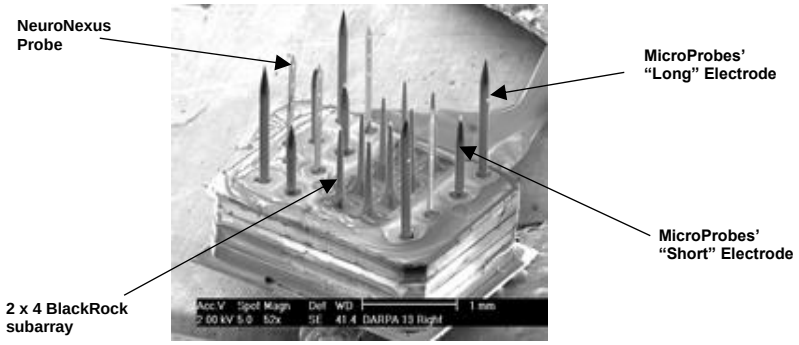

FIGURE 2.1. An SEM image of hybrid array

Fully anesthetized animals were transcardially perfused using a published perfusion protocol as described in (Han, Manoonkitiwongsa, Wang, & McCreery, 2012). The implanted device was carefully removed and a tissue block of 6 mm x 8 mm x 10 mm was punched out. Serial sections of 50 µm thickness were sectioned perpendicular to the electrode shanks till a depth of 3 mm. Up to 40 slices for each array block to capture regions of interests (ROIs) above and below the individual electrode tip site.

2.1.1 Immunohistochemistry

The tissue sections were stained with immunofluorescence labelling procedures as described in (Duong & Han, 2013)**.** Below is a table (TABLE 2.1.1) indicating the list of antibodies and their corresponding stained cell types.

Table 2.1.1: List of antibodies and stained cell types

ANTIBODY (FALSE COLOR)	STAINED CELLS
GFAP (Green)	Reactive Astrocytes
NeuN (Purple)	Neuronal nuclei
IBA-1 (Red)	Macrophages
MAP-2 (Blue)	Neuronal Dendrites
DRAQ-5 (Cyan)	Nuclear stain (all cell bodies)

2.1.2 Image acquisition

Fluorescently-labeled, serial tissue slices were imaged using an LSM 510 Meta laser scanning system. Multiple fields of view were scanned automatically. 100 fields-of-view FOVs were scanned with a 10% overlap between adjacent tiles to allow for stitching. The optical slice thickness was 3 µm. All electrode tracks were included in the scanned area of each optical slice during the confocal scanning.

All of the above was carried out at the Huntington Medical Research Institutes, Pasadena, California.

2.2 Image Processing and 3D reconstruction workflow

The 3D reconstruction for this thesis has been carried out for a tissue block of the right sensorimotor cortex of one cat. The scanned tissue volume included sufficient grey-matter cortical depths encompassing all of the electrode tips in the hybrid array. FIGURE 2.2 is a schematic of the steps involved in the 3D reconstruction of the intracortical volume. The confocally scanned images are first stitched in the x-y plane (a - b). Then, each confocal 3D stack consisting of multiple 3 µm thick optical slices to form a section of 50 µm thickness is stacked upon the consecutive confocal 3D stacks to form one 3D volume (c). Post-processing, i.e., after applying dewarping, intensity normalization and alignment, a 3D registered volume can be obtained (d-e). All the steps of the reconstruction workflow are described in detail in the succeeding pages.

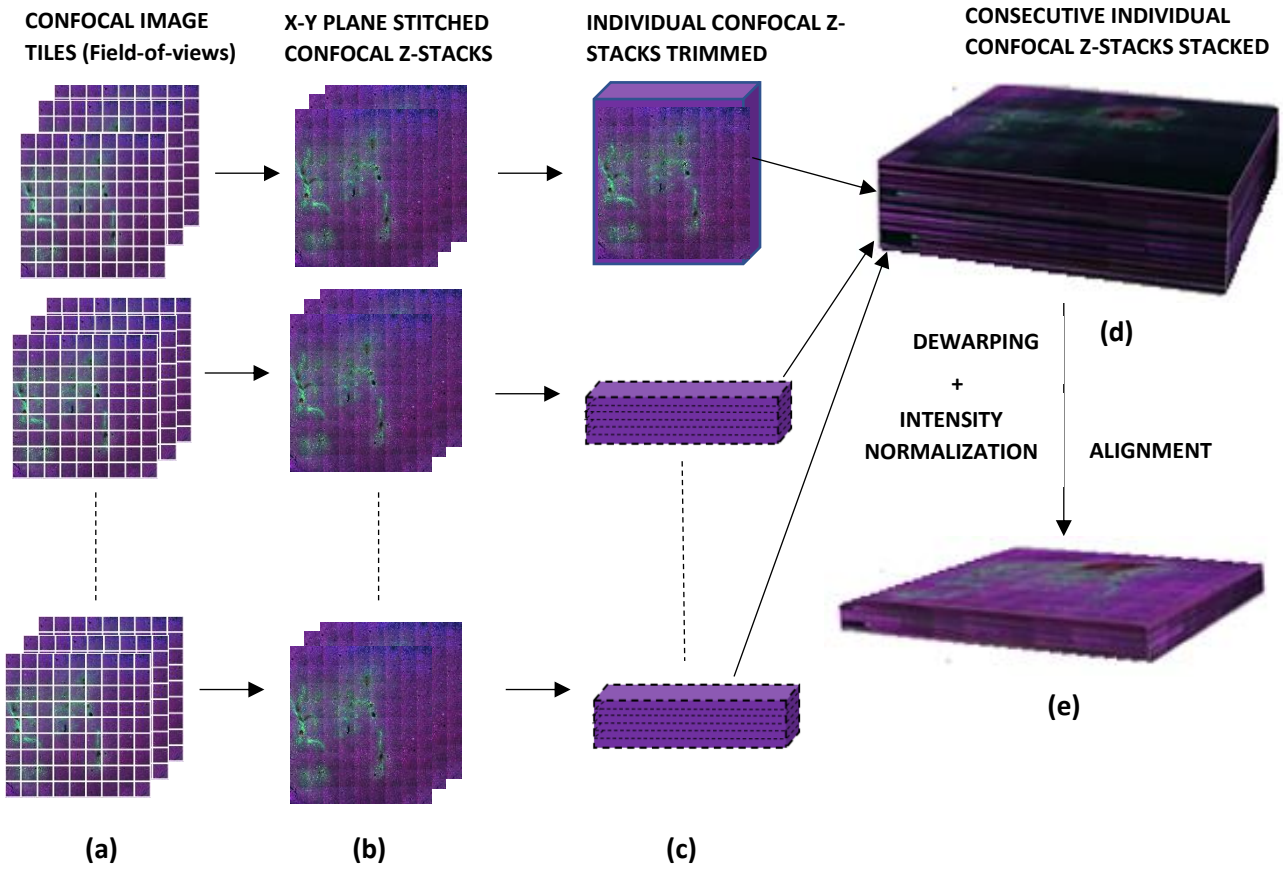

FIGURE 2.2 Schematic of workflow for 3D image reconstruction illustrating (a) confocal image tiles, (b) stitching of fields-of-views, (c) individual confocal z-stacks after trimming to the same x and y dimensions, (d) entire volume of stacked individual confocal z-stacks, and (e) the final 3D volume after dewarping, intensity normalization and alignment.

2.2.1 Stitching

Stitching is done using XuvStitch™ (XuvTools) (FIGURE 2.2 (a) and (b)). Individual image tiles are stitched using automatic mode: ten percent overlap and ninety-five percent similarity threshold. Manual Stitching is used for seamless stitching in case automatic mode is not adequate. Z-adjustment can be applied to correct out-of-focus optical slices and z-axis shifting. However, for our dataset we did not use the z-adjustment as the dewarping algorithm applied at a later stage of the image processing workflow helps in correcting the z-axis shifting. We noticed that applying a z-adjustment within the software

while stitching sometimes introduced a fringe pattern on the side of the stitched image which could affect the accuracy of quantification at a later stage.

2.2.2 Trimming and Stacking

The physical sections of 50 µm need to be stacked together to form the whole 3D volume using Imaris (FIGURE 2.2 (c) and (d)). Fourteen physical sections encompassing the electrode tip holes were to be stacked. The resolution of the largest individual section for stacking is 4553 x 4658 x 297 voxels and the dimensions for each voxel is around 0.89 µm x 0.89 µm x 3 µm. A condition for stacking the optical sections is that their X and Y dimensions must be equal. There were some inconsistencies in the X and Y dimensions due to manual nature of physical punching out and serial sectioning of the tissue block before mounting on the slide for the image acquisition process. Once the images of the sections are acquired, the X and Y dimensions of each section is noted and all the sections are cropped or trimmed so that all of them have equal X and Y value. This trimming is minimal outside of the regions of interest, i.e., outer perimeter of the array, and does not cause loss of data. The sections are ultimately trimmed to a resolution of 4,093 x 4,184 x 297 voxels with the same voxel sizes of 0.89 µm x 0.89 µm x 3 µm. Once this step is done, the optical sections can be stacked up on top of each other to create a continuous 3D volume. FIGURE 2.2.2(a) and (b) illustrate images of different views of the image data after trimming and stacking. FIGURE 2.2.2 (c) and (d) show sample images of stained cell types obtained.

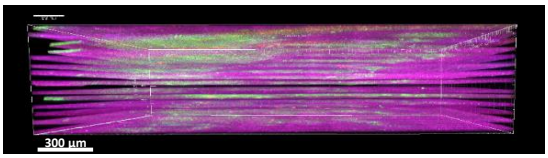

(a)

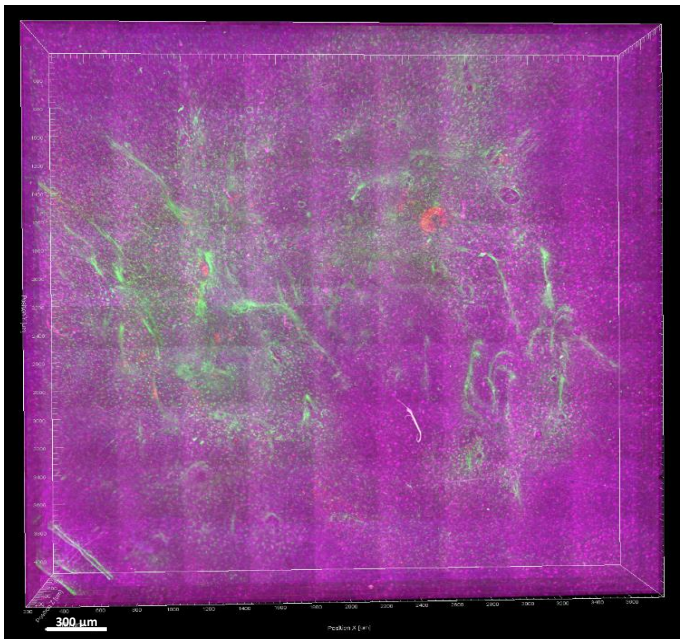

(b)

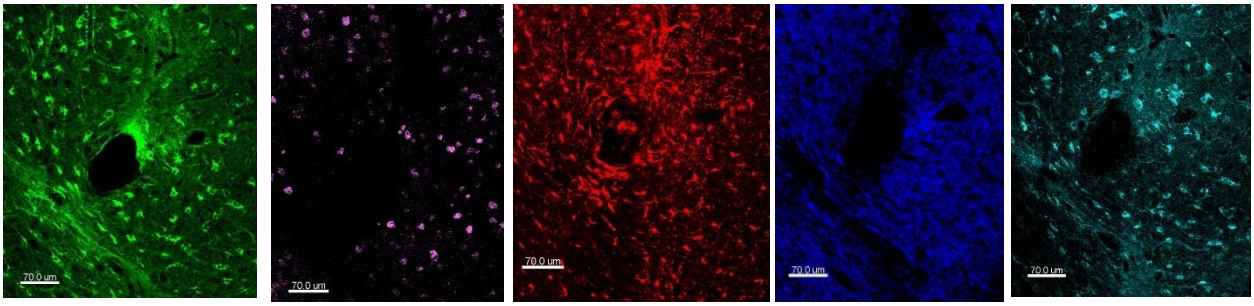

(c)

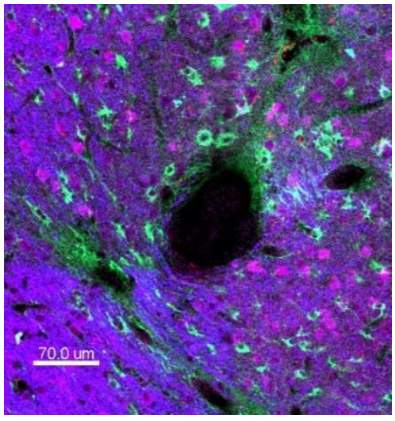

(d)

FIGURE 2.2.2 (a) A front view of the trimmed and stacked raw 3D volume in the x-z plane, (b) a top-down view of the trimmed and stacked raw 3D volume, (c) raw individual channel images showing staining information (Left to right – GFAP, NeuN, Iba-1, MAP-2 and DRAQ-5), and (d) top-down view of all the five color channels showing the combined staining information around a ghost electrode hole.

2.2.3 Dewarping

Dark bands between sections of the aligned stack were observed possibly due to tissue deformations during sectioning and mounting on glass slide and image acquisition artifacts. We applied a custom-built dewarping program interfacing MATLAB (The MathWorks, Inc.) and Imaris (Bitplane AG), to eliminate completely dark slices and normalize the intensities of the slices in the stack.

For this feature, the user is required to provide an input of the number of optical slices per section the user wants to keep. We chose sixteen slices per section because the tissue block was sectioned at 50 µm thickness. Each optical slice is 3 µm thick, hence 16 x 3 µm = 48 µm ~ 50 µm, i.e., the physical section thickness.

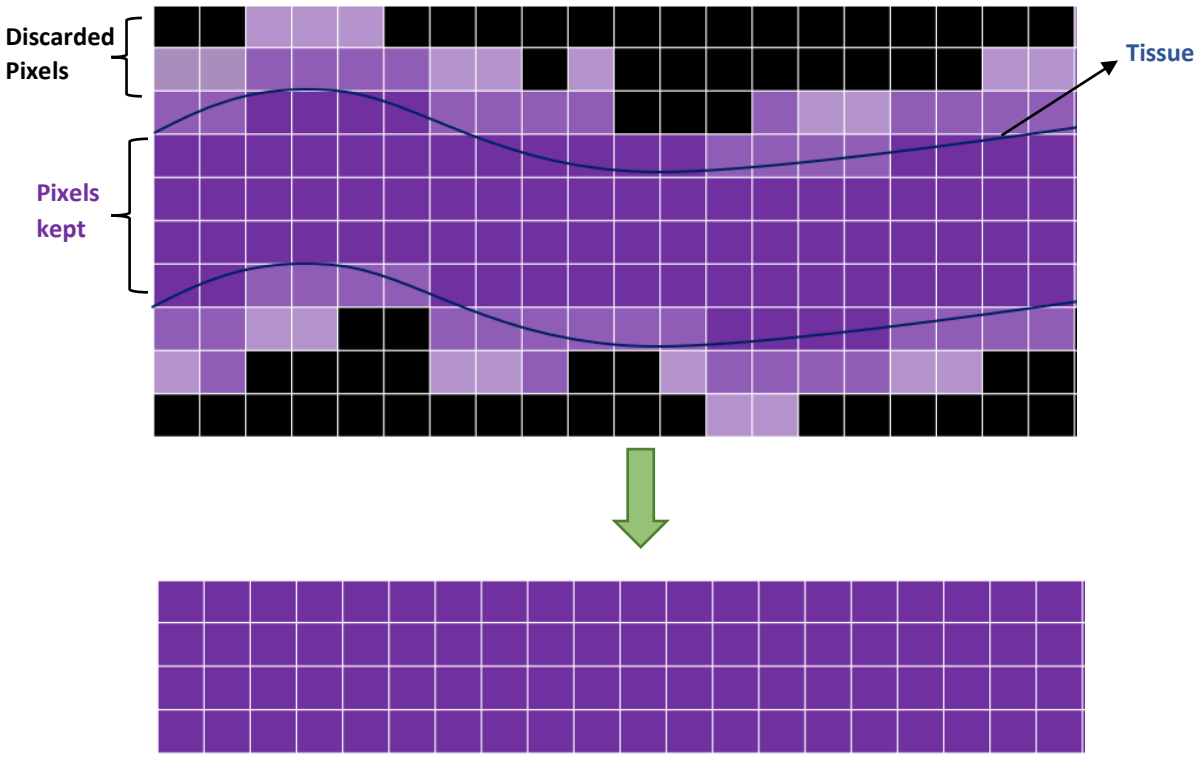

(a)

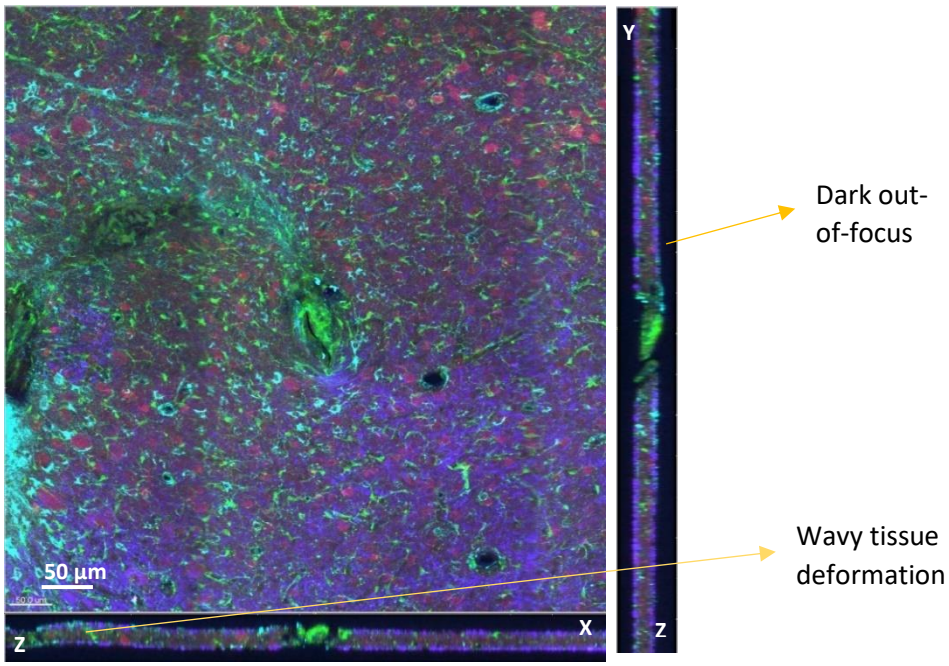

(b)

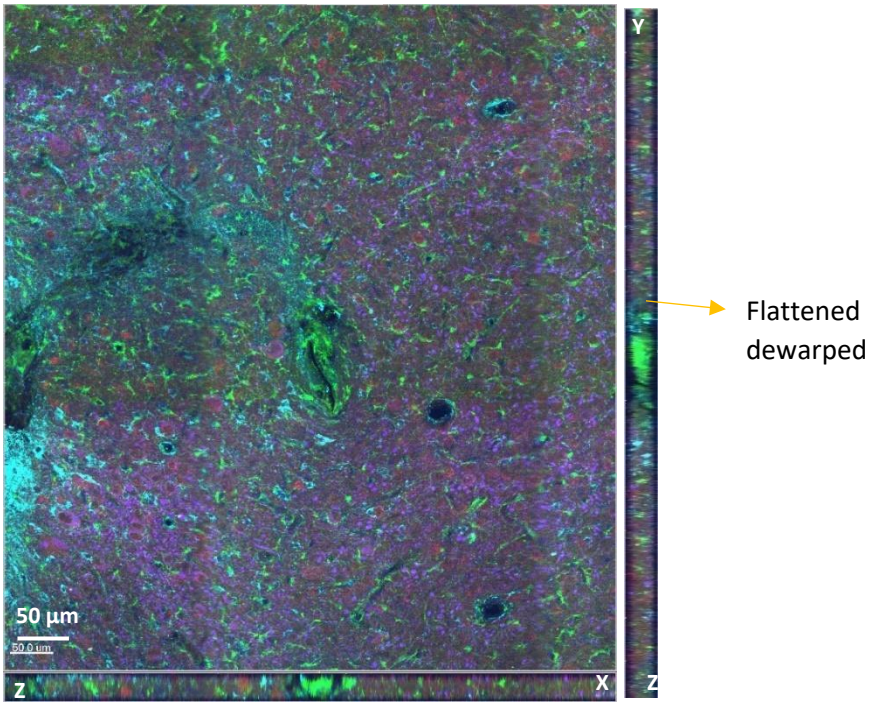

(c)

FIGURE 2.2.3 (a) A Schematic of the working of the dewarping algorithm. Brightest subset of contiguous pixels is retained to form a flatter section (developed by Nolta et al., unpublished), (b) Before dewarping, showing dark regions and curved tissue section, and (c) After dewarping, showing a planarized tissue section.

The algorithm then chooses the brightest subset of contiguous pixels in each z-column and retains them, while discarding the other low intensity pixels. The dark slices with no useful information encompassing dark, out-of-focus pixels are removed and the tissue deformation is also fixed as can be seen in FIGURE 2.2.3 (a). Dewarping the stack not only helps in giving a more accurate and aesthetic data set, but also helps in manually aligning the slices better. An additional step of normalizing using an in-built function of Imaris is also applied. The improvements in the image quality can be seen in the before and after images in FIGURE 2.2.3 (b)-(c).

2.2.4 Alignment

Next, a manual alignment of the stacked and dewarped image dataset can be done using a 3D image registration and alignment software called AutoAligner (Bitplane AG). This software has both automatic and manual alignment mode. However, automatic alignment works best for image data having well-defined and continuous fiducial markers. We applied manual translational and rotational transformations by focusing on Microprobes and Blackrock array shank holes that we intended to perform our quantification and analysis on. Certain tissue deformations in the x-y plane such as stretches and compressions while sectioning and mounting of the tissue on the slides may hinder the perfect alignment of all the shank holes. Hence, the marker for good alignment is aligning at least two shank holes in the best possible way. During the alignment, it is noticed that the shank holes in each physical section are not in a perpendicular straight line and shift slightly to one side indicating that there is a shift in the electrode shanks although the electrode array was mounted perpendicularly into the

animal brain. This tilt or displacement of certain electrodes, thus tissue slashing, may be primarily attributed to: (1) bending of individual electrode shanks during surgical insertion which is likely with NeuroNexus shanks, (2) the force exerted chronically by connective tissues around cables thus pulling and tipping the array, and (3) the non-ideal extraction of the brain regions with respect to the directions of the shanks of the array.

AutoAligner allows us to load the whole dataset and manually align it. However, a major problem with this software is that it does not allow us to apply the alignment changes to the entire dataset (i.e., it crashes for image dataset files larger than 12GB). To work around this issue which is central to our 3D reconstruction effort, we integrated MATLAB (The MathWorks, Inc.) programming and Imaris (Bitplane AG) through a multi-functional two-way interface called ImarisXT to align the whole dataset. This way, we can load the entire dataset, carry out manual alignment once and apply the ImarisXT function to align the entire dataset. Once the manual alignment for the whole dataset is carried out in AutoAligner, an alignment file (.txt) consisting of corresponding translation and rotation coordinates of each optical slice of each physical section is saved. Using MATLAB, the contents of the alignment file are extracted and stored in transformation matrices. A transformation matrix ideally looks like:

$$\begin{bmatrix} \cos\theta & -\sin\theta & x \\ \sin\theta & \cos\theta & y \\ 0 & 0 & 1 \end{bmatrix}$$

where x and y are the translational coordinates and θ is the angle of rotation of the slice. The alignment file extracted from AutoAligner consisting of matrices for each optical slice has some additional information including the value of θ which can be directly extracted. The transformation matrix from AutoAligner looks like:

$$\begin{bmatrix} \cos\theta & -\sin\theta & x & X \\ \sin\theta & \cos\theta & y & Y \\ 0 & 0 & 1 & \theta \end{bmatrix}$$

where X and Y are the dimensions of the image and the angle of rotation is given in the 4 x 4th element. Some additional coordinate values such as x_{min} and y_{min} appear in the beginning of the extracted file and AutoAligner uses these values as the center of rotation. Imaris is interfaced with MATLAB, the full uncropped data is sent to MATLAB, the edges of the images are padded with additional pixels to provide additional space to accommodate the rotational and the translational effects of the alignment around the edges, the transformation matrix is applied to the padded image dataset and the aligned 3D image montage is sent back to Imaris. FIGURE 2.2.4 shows aligned electrode tracks.

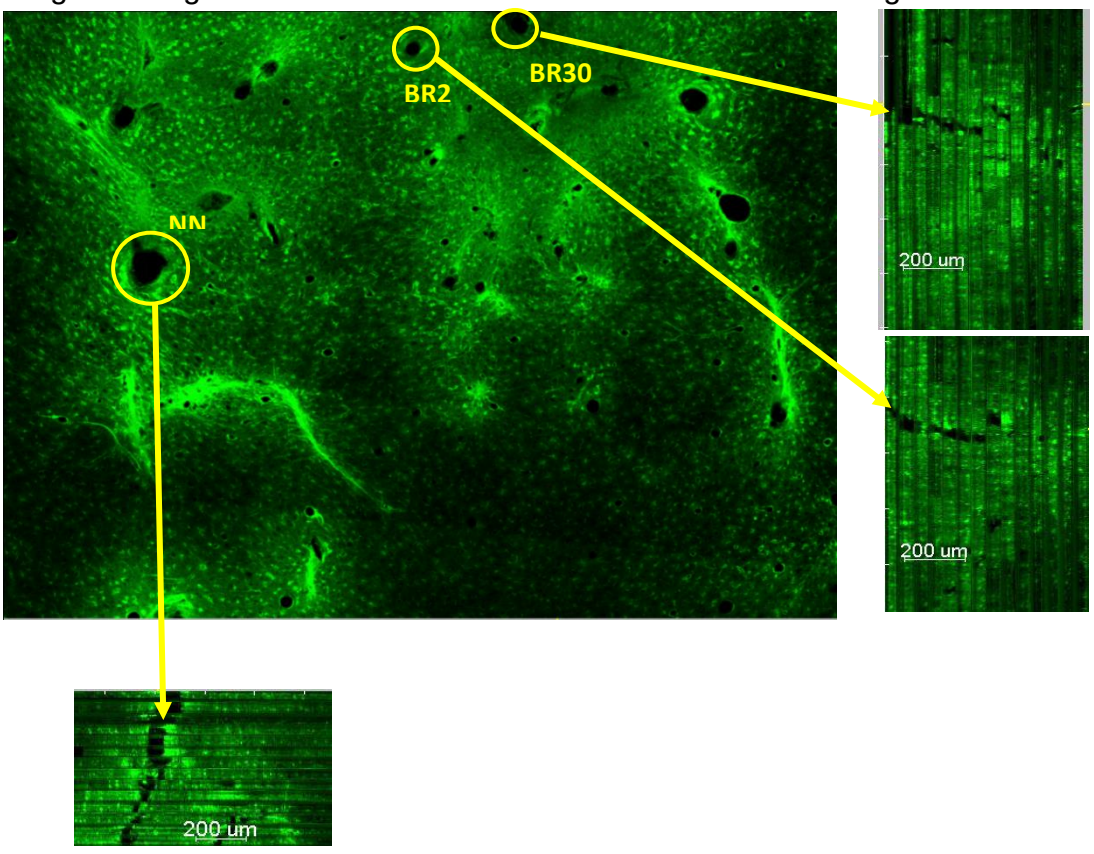

FIGURE 2.2.4 (GFAP staining only indicating astrocytes) XY view of one slice indicating 3 shank holes (NN1 – NeuroNexus probe, BR29 and BR30 – Blackrock probes). XZ view shows the aligned electrode tracks for NN1. YZ view show the aligned electrode tracks for BR29 and BR 30.

2.3 Quantification

Quantification was carried out for three Blackrock electrode tips and one short Microprobe microwire in the hybrid array. Different distance bins were created around the shank in increments of 25 µm up to a distance of 200 µm, for quantifying the densities of neurons, and astrocytes around each electrode type. All of the quantification steps that follow was carried out using different modules of Imaris for detecting and rendering different structures in the 3D volume.

2.3.1 Drawing the electrode tips

The data set is converted from 16-bit to 32-bit before drawing the shanks. This is a requirement for the distance transform functionality. Also, it is down-sampled by fifty percent because the files were too large for distance transformation at a later stage. Artificial shank tips were created using the “surfaces” feature of Imaris. Shank tip lengths for the Blackrock electrodes and the microwire short electrodes were previously measured under an optical microscope during device fabrication. Using this information, the section of the volume at which the shank tip begun was determined by looking backwards from the slice where the ghost shank hole disappears in the volume. The GFAP traces of astrocytes were used as an indicator of where the ghost shank tips disappeared. The “circle” drawing mode is used to draw the shanks and 100 vertices are chosen for each circular contour which provide smoother outer zones. Once the contours are drawn on sequential slices, the software builds the shank by connecting the contours. Care must be taken to ensure that adequate contours are drawn for slices skipping only a small number of slices in between, to form one single continuous surface.

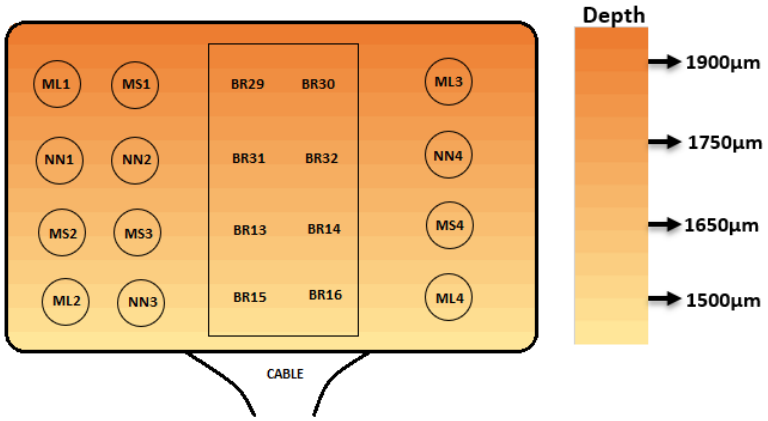

FIGURE 2.3.1.1 A schematic of the hybrid array with heat map indicating the depth of electrodes in the intracortical space due to tilting (BR - Blackrock, MS – Microwire Short, ML – Microwire Long, NN – Neuronexus).

Eight Blackrock electrodes and two microwire short electrodes are drawn this way. A tilt in the orientation of the electrode array can be noticed when these shanks are drawn. The end of the electrode array attached to the cable is shallower while compared to the other end of the array as indicated FIGURE 2.3.1.1 and this is evident in the 3D volume in FIGURE 2.3.1.2.

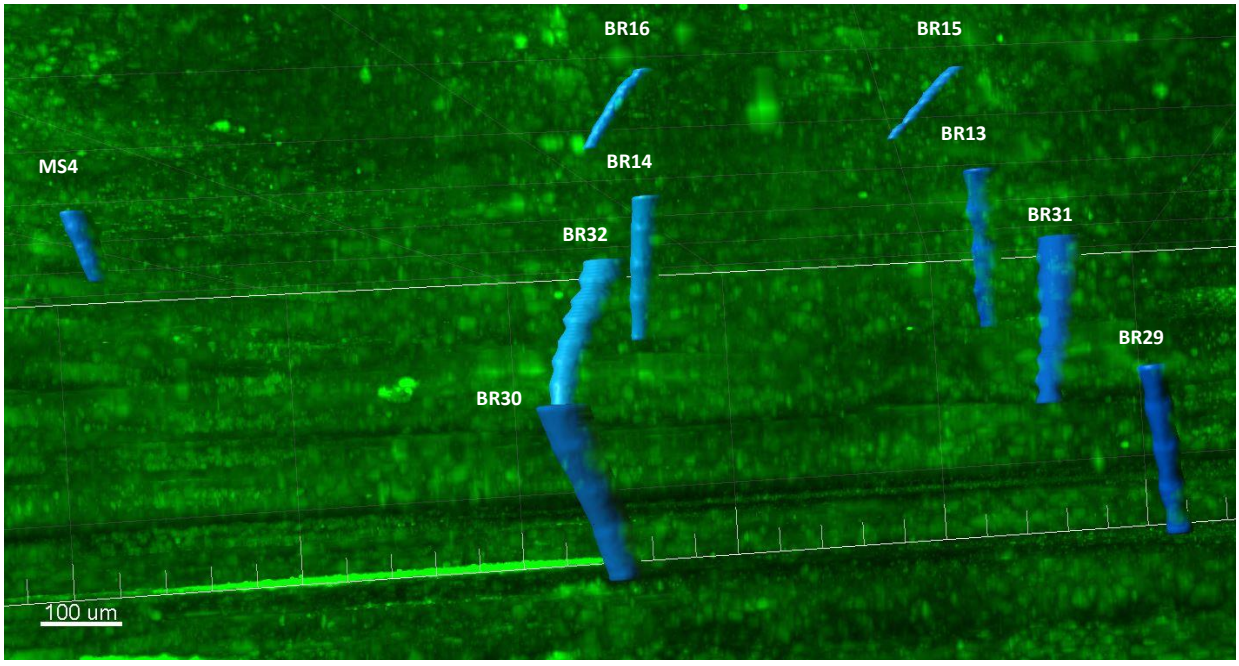

FIGURE 2.3.1.2. A global view of artificial shanks in the 3D reconstructed volume.

2.3.2 Applying distance transformations

Distance transformations are applied to each shank. A new color channel for the distance transform to the shank is created. Surfaces are rendered around the shank to create distance bins in increments of 25 µm, up to a distance of 200 µm. The NeuN and GFAP channels are masked around the shank using this method to create distance bins for neuron and astrocyte detection and quantification as can be seen in FIGURE 2.3.2 (a) and 2.3.2 (b).

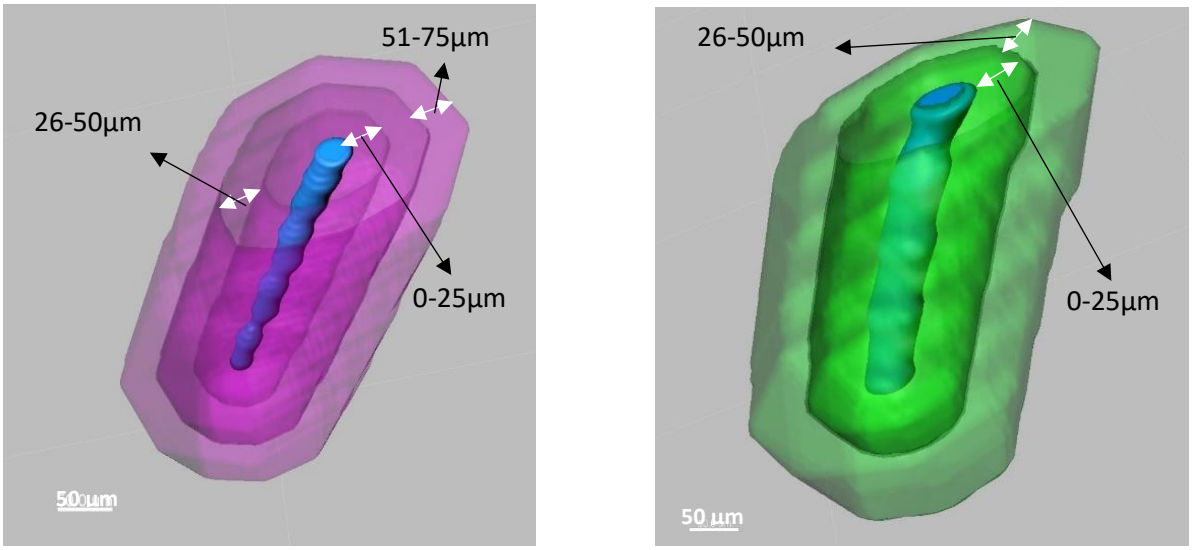

(a) (b)

FIGURE 2.3.2 (a) distance transformed bins for NeuN channel for spot detection. It is generally believed that neuronal activity within 100µm from the electrode surface can be sensed and (b) Distance bins for GFAP channel for spot detection.

2.3.3 Neuron Detection

The automatic spot detection feature and the filament tracing feature of Imaris was used to render neuronal nuclei and astrocytes marked by NeuN and GFAP, respectively. This feature provides more reliable quantification than intensity-based quantification since non-uniform staining quality within a tissue section and also across batches. Neuronal nuclei are easily distinguisable by high intensity blobs in the 3D volume having a diameter

of about 10 µm or higher. This diameter was manually measured for multiple neuronal nuclei in the 2D slice view of the 3D volume (FIGURE 2.3.3 (a)). Intensity mean thresholds were applied to include spots only in a certain range of values. Any false negatives were manually removed after the automatic detection. Finally spots are rendered as can be seen in FIGURE 2.3.3 (b).

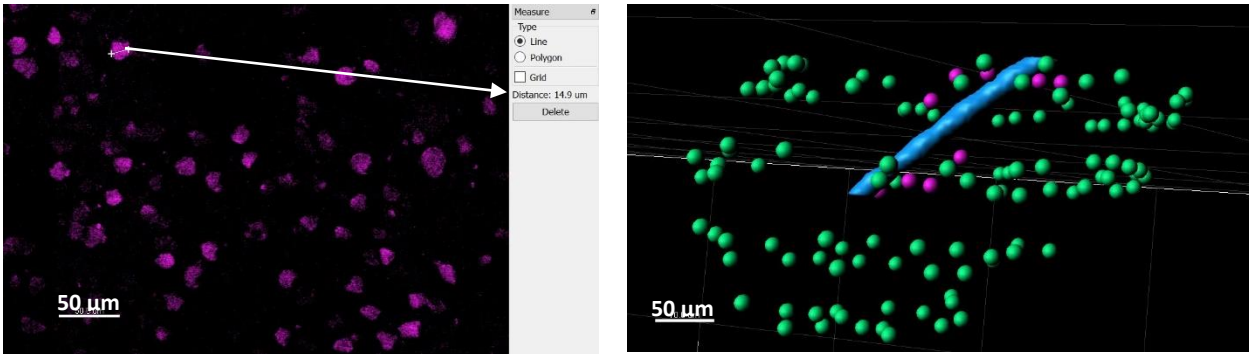

(a) (b)

FIGURE 2.3.3 (a) Slice view of NeuN stained tissue to estimate diameter of a neuron and (b) Spot detection functionality detects and places a sphere in the place of a 10 µm diameter blob.

2.3.4 Astrocyte Detection

The astrocytes were rendered using the filament tracing feature wherein we have to define the starting (largest) diameter and the ending (smallest) diameter of the filament. A value of 10 µm was used for the largest diameter based on manual measurements in the slice view and for the smallest diameter, a value in the range 0.8 – 1.8 µm was used. Additional intensity thresholds can also be defined for the detection. Finally, a fibrous mesh of astrocytes is rendered as can be seen in FIGURE 2.3.4.

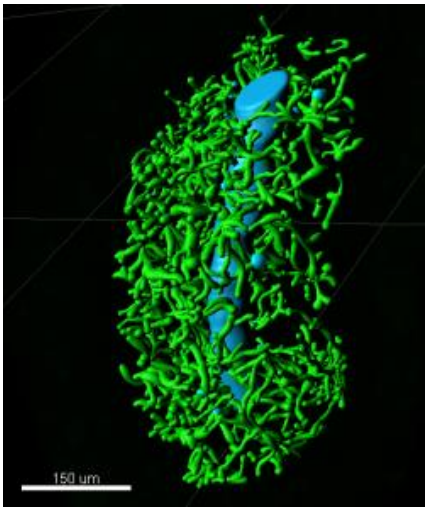

FIGURE 2.3.4 Astrocytes (green) traced up to 50µm around an electrode tip (blue)

CHAPTER 3

RESULTS

3.1 True 3D Alignment of Brain Tissue in Its Entirety

The alignment of whole uncropped data is now possible using AutoAligner (Bitplane AG) and custom-built program in MATLAB (The MathWorks, Inc.) to carry out fiducial-based alignment. Previously, we were required to crop sub-regions of the entire dataset around two shank holes each for reliable alignment and to generate smaller files that AutoAligner can handle. Manual alignment was needed each time for each sub-region and applied to the dataset. Each hybrid array has twenty electrodes around which quantification needs to be carried out. This meant that the cropping and manual alignment of each sub-region needs to be repeated nine more times to be able to quantify around all the twenty electrode tips for each dataset. This process was tedious, cumbersome and time-consuming. Also, it did not allow us to have a holistic visualization of the quantifications around each electrode tip of the hybrid array in the whole 3D volume simultaneously. We have approximately twenty-two such image datasets that we intend to analyze in the future and the old method would have been extremely labor-intensive.

However, with the new improvement in the alignment method for datasets larger than 12 GB will enable us to save time and align all electrode tracks at once.

3.1.1 Computational costs of the alignment of the 3D volumetric sections

The manual alignment is a common step for the previous and the current method of alignment. It takes around 2-3 hours for an individual who is familiar with the dataset and its fiducials for alignment of, approximately 14 consecutive sections. Once this manual alignment is done, previously, the changes were applied and saved to the sub-cropped regions of data within AutoAligner. This step takes about 2 hours for each sub-cropped region (i.e. a total of approximately 20 hours for each dataset), has a maximum CPU usage of 47%, and uses physical memory of about 85 GB out of 176 GB (48% of RAM). Currently, the algorithm written to align the whole uncropped dataset takes a total of 11.74 hours. The block of code that takes the longest time (96%) is when the images are being sent back and forth between Imaris and MATLAB and the rotational and translational effects are being applied to the images and about 2.5% of the time is for padding data around the images. Also, maximum CPU usage (about 98%) occurs during this step and around 20-21GB of the physical memory (11-12% of RAM) is used during the execution of the algorithm. The new method of alignment is about twice as fast as the old method. Below is a table (see TABLE 3.1.1) consisting of a breakdown of the amount of time taken up by the major steps in the alignment algorithm. The first row has timings for the entire dataset used here and the second row has timings the algorithm takes for applying alignment coordinates for any two consecutive sections.

TABLE 3.1.1. Time (in seconds) taken by each block of code in the alignment algorithm

Number of sections	Total Number of Slices	Padding Data in Imaris (in seconds)	Obtaining new padded data in MATLAB (in seconds)	Applying rotational and translational effects (in second)
14	224	1044.84	37.55	40964.19
2	32	113.00	4.78	1195.63

3.2 3D Realization of Active Electrode Surface and Functional Ramification

Given that only the active, deinsulated surface of microelectrodes is capable of recording neuronal signals, a more realistic drawing of artificial electrode tips in Imaris using the surfaces feature is important and has been possible in this study. Previously, 10 vertices were used to draw the contour lines on sequential slices to create the electrode tip. However, once distance bins are created by expanding outward to, for example, 75 µm and 100 µm, the distance bins formed very jagged edges and not smooth circular distance bins like we would desire. Choosing a higher number of vertices improves this jagged appearance of distance bins. This new feature provided a more accurate count of number of neurons measured radially from the electrode tip. This is particularly important in the three-dimensional space. With 100 vertices, the distance bins do not have such spiky corners around the edges and are much smoother.

3.3 Measurements and Quantifications in 3D Brain Volume

Neuronal densities were calculated by counting the number of neurons around the electrode tip and below the electrode tip and dividing the total number of neurons by the volume of the respective distance bin (FIGURE 3.3.1). For Blackrock electrodes (n=3), the neuronal densities in the immediate vicinity of the electrode tips is found to be low, compared to distances more than 100 µm away from the electrode tip. For microwire short electrode tips (n=1), the neuronal density is low near the electrode tip and is higher at a distance more than 100 µm away from the electrode tip site.

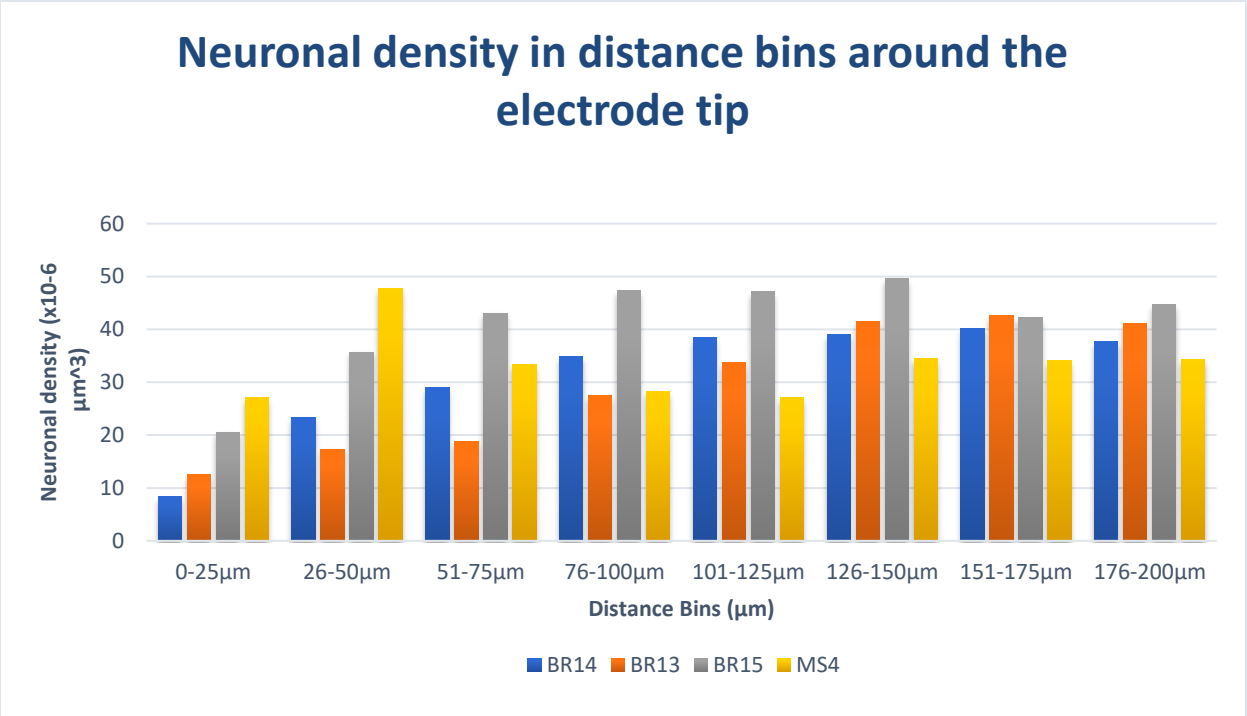

FIGURE 3.3.1 Neuronal density for three Blackrock electrode tips and one short Microwire electrode tip. For Blackrock (BR), increasing neuronal densities are calculated as the distances increase from the electrode surface. A similar pattern was found for the MS4 electrode, with a higher neuronal density in the 26-50 µm bin.

For astrocytic scar tissue formation, the volume of all the filaments formed in each bin was divided by the volume of the distance bin to find the volume density of the astrocytes

(FIGURE 3.3.2). For Blackrock electrodes (n=3), the astrocytic volume density is high close to the electrode site and decreases after a certain distance of around 50-75 µm.

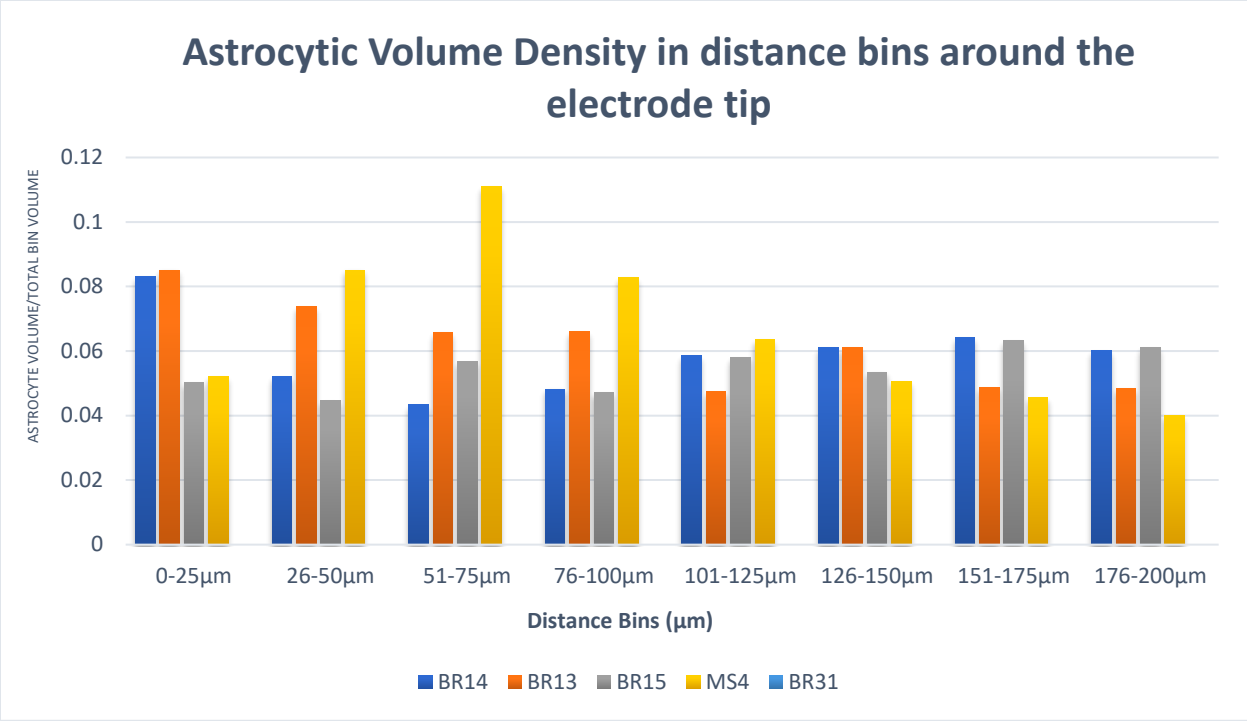

FIGURE 3.3.2 Astrocytic Volume Density for three Blackrock and one short Microwire electrode tip. The astrocytic scar tissue density is highest in the 0-50 µm range for Blackrock microelectrodes and in the 0-75 µm for Microwire electrode tips.

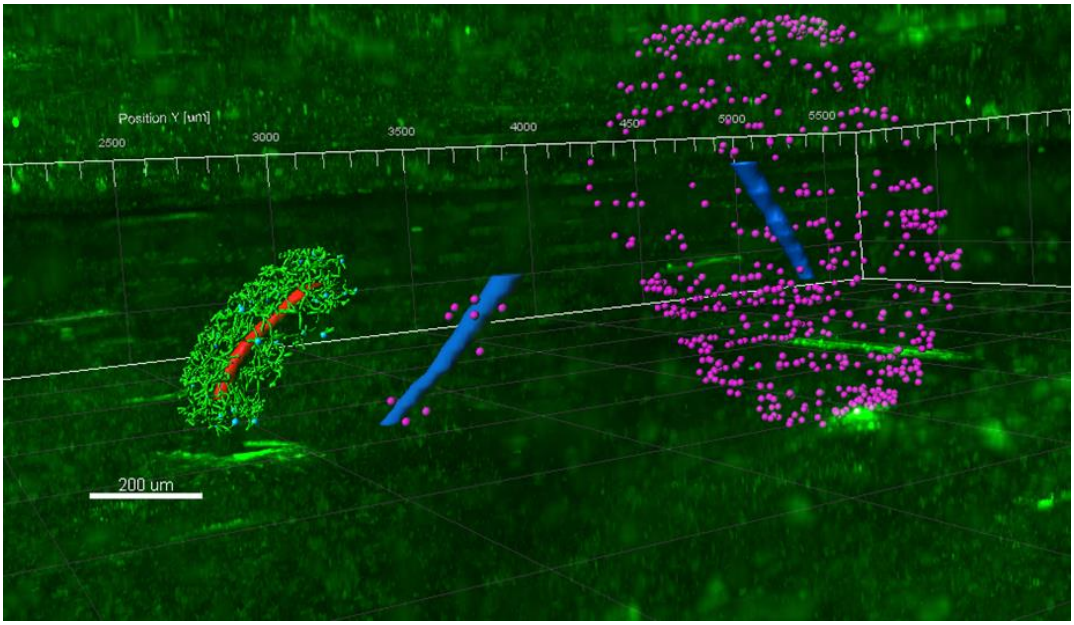

FIGURE 3.3.3 An illustration of three Blackrock shank tips with astrocyte tracing (green GFAP) and neurons (magenta NeuN) detected in the true 3D reconstructed volume (green GFAP channel).

CHAPTER 4

DISCUSSION AND FUTURE WORK

The improvements to the 3D tissue volume reconstruction workflow, drawing of artificial electrode tips and quantification of neurons and astrocytic scar tissue was successfully carried out. This represents the first demonstration of a truly 3D reconstruction and quantification of neuronal and glial cells around the active surfaces of microelectrodes. Coupled with the hybrid array's components which represent a majority of all neural interfaces used in the field, this work is poised to provide realistic and powerful computing tools that will bridge the gap that exists between the unstable electrode to neural tissue interface chronically and the limited 2D visualization of the tissues currently being conducted in the field.

However, there were some limitations encountered during this process. The section-by-section alignment of the tissue block was achieved for the whole uncropped data. Yet, we noticed some local stretching and compressions in the X-Y plane. FIGURE 4.1 (a) shows some remaining local misalignments even after rotational and translation

alignment adjustments were applied. This is due to local shrinkages and expansions in the range of 3-20 µm between shank holes that can be seen in FIGURE 4.2 (b) and FIGURE 4.2 (c). These stretches and compressions are most likely caused during the staining of the tissues that involves solvents and heat treatments. The rotational and translational changes applied in the AutoAligner program only takes care of alignment issues due to change in direction or shift. There is a need for non-rigid alignment that will enable us to compensate for local stretches and compressions that occur due to a variety of factors during tissue processing and sectioning (Jimson, Malathi, Kailash Kumar, & Balachander, 2016).

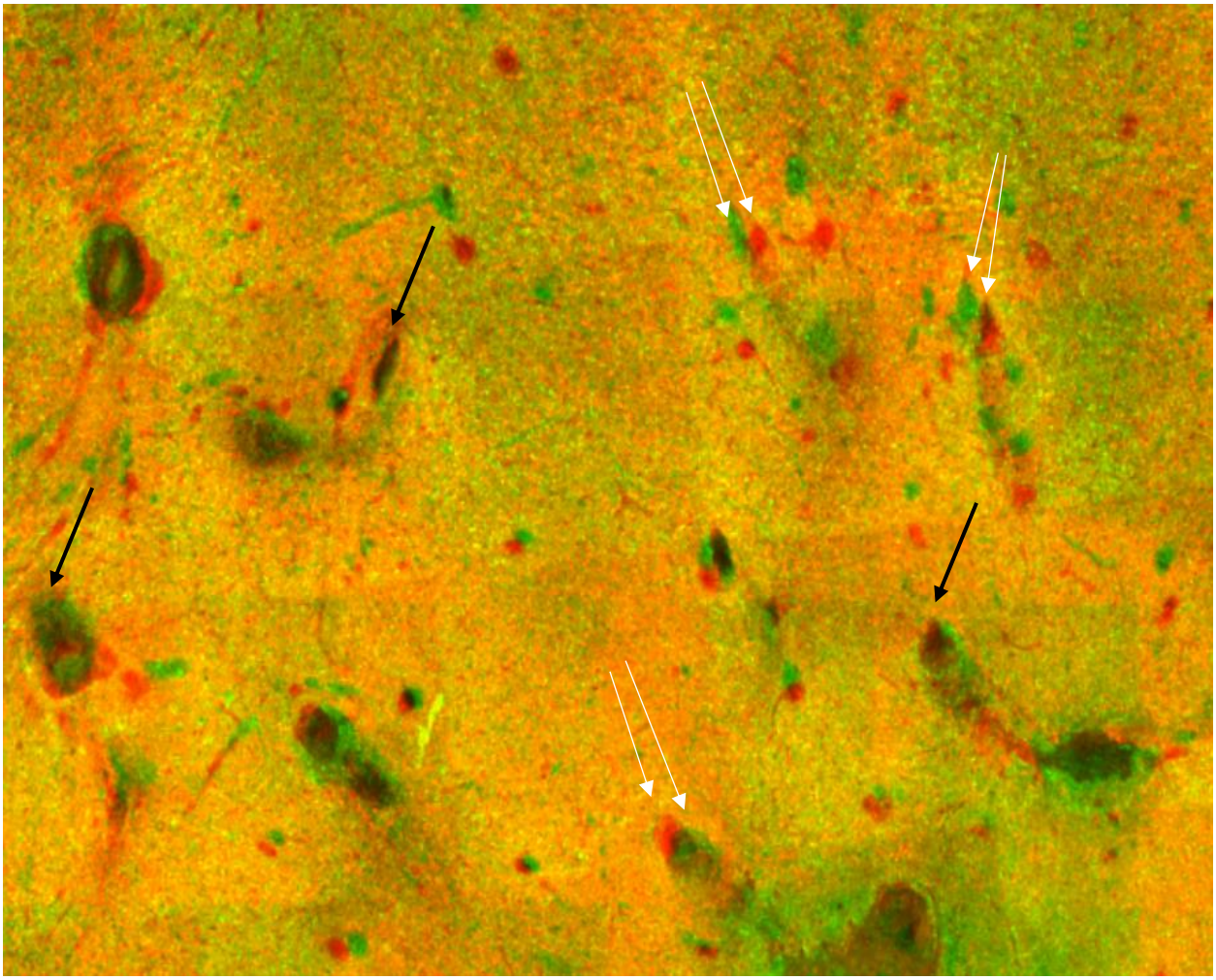

(a)

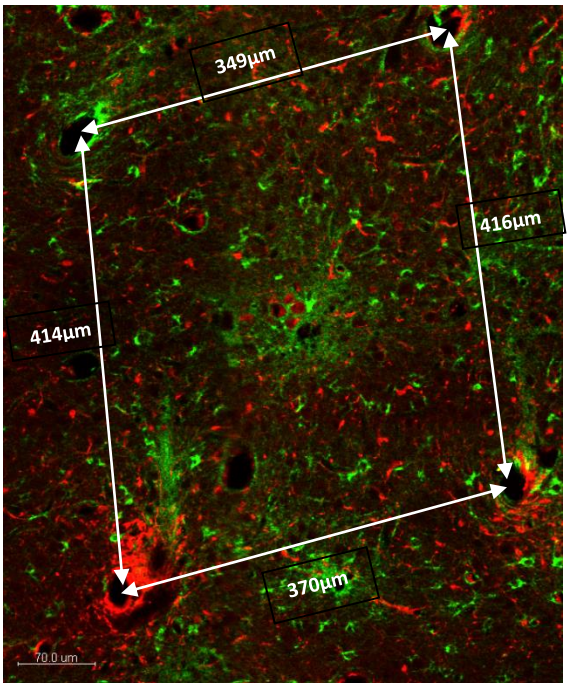

(b)

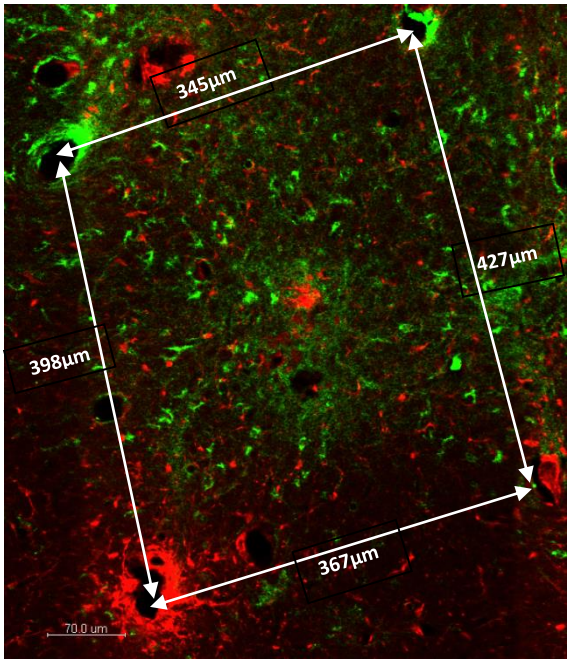

(c)

FIGURE 4.1 (a) Top most slice of one section overlapping with the bottom most slice of the consecutive section. Black arrows indicate well aligned fiducials whereas White arrows show unaligned fiducials, (b) An optical slice from the 3rd physical section of the dataset, and (c) An optical slice from the 4th physical section of the dataset, illustrating even the vertically-adjacent sections have distorted dimensions.

In one study, authors used accurately-matched feature pairs for fast and a high level automatic coarse registration (Wang, Ka, & Chen, 2014). Data normalization is used to reduce stain variations and enhance tissue patterns to identify features for registration. Grids are placed over the source and target images intended to be registered and a deformation field is calculated from a deformation grid to align the two images perfectly. This could be one direction for an automatic registration, however care must be taken to ensure that the fiducials are correctly detected. Another approach would be to manually stretch and compress the slices locally as required (Koshevoy, Pavel & Tasdizen, Tolga & Whitaker, Ross & Jones, Bryan & Marc, Robert, 2008). In this study, they have attempted to processes large (terabytes) datasets. A custom-built user interface is used to manually tweak the local distortions to enable smooth slice-to-slice registration. The

algorithm uses an elastic transformation based on thin-plate spline technique.

FIGURE 3.3.2 and 3.3.3 showed a similar trend as previously reported in the literature in that: (1) the neuronal densities in the immediate vicinity of the electrode tips is found to be low, compared to distances farther away, and (2) the astrocytic volume density is high close to the electrode site and decreases after a certain distance (Downey et al., 2016)(Downey et al., 2016). However, there were small differences between Blackrock and Microwire electrodes. One thing to note is that the Blackrock electrode had more variations in electrode surface areas compared to those of the microwires which were more uniform. Additional quantification around many more electrode sites would be required before a definitive conclusion could be drawn.

The hybrid array consists of four different kinds of probes, one of which is the NeuroNexus probe which is 1.5 mm in length. These are multi-site electrodes and have a different shape compared to the other electrodes in the hybrid array. They have a flatter rectangular geometry cross-sectionally and are not needle-like electrodes. The electrode tips can be drawn using the ‘click’ mode of the surfaces. However, the bigger challenge will be in determining the electrode sites along the shank as they are not obvious depth information in the tissue volume. A well-registered 3D volume with well-defined depth fiducials using adjacent tip-based electrode can help in locating the microelectrode sites.

Based on some of these techniques, in the future, we hope to incorporate corrections for local tissue shrinkages and expansions to our 3D reconstruction process. Once this approach is fine-tuned, we will be able to extend this 3D reconstruction software to quantify foreign body response, neurons, and nerve fibers, not only deep within the brain, but also in the spinal cord and in the peripheral nervous system. The spinal cord has grey

and white matters through which the cross-sectional dimensions change over length. Similarly, peripheral nerves travel over a distance and an analysis using a 3D reconstructed volume would be more comprehensive. This reconstruction process can serve a wide-range of image datasets as it is not specific to our dataset, but more generic to solve the most commonly encountered image artifacts.

Tissue clearing is becoming a key technique for three-dimensional imaging of a large volume of tissue (Azaripour et al., 2016; Vigouroux, Belle, & Chédotal, 2017). This could mean we will not require sectioning and reconstructing tissue blocks in 3D. Optical clearing agents are used to make the tissue transparent facilitating three-dimensional microscopy of the tissue. CLARITY is a tissue clearing technique that is gaining a lot of popularity and many research groups are working on improvising this technique. However, there are still some issues with tissue clearing. Protein losses resulted during tissue clearing: approximately 8% for the CLARITY method and higher for some other clearing methods (Azaripour et al., 2016). Penetration of anti-bodies might prove difficult and there might be a necessity of a pretreatment of the tissue section to improve penetration. Also, acquiring the 3D image is complex because of the size of the large dataset and its complexities. Non-uniform tissue clearing could potentially pose a problem in the image acquisition for tissue volumes that have holes due to explanted electrodes (Richardson & Lichtman, 2015). Hence, tissue clearing techniques need a lot of improvements before they can be used to image tissue volumes for accurate quantification and analysis.

So far in this study, the quantification process was carried out only for four out of twenty electrodes in the hybrid array. A larger sample size is required to make accurate

conclusions about the effects of foreign body response on the chronic performance of the different types of electrodes. Since these were recording electrodes, the results of the histological analysis of the tissue around the electrode tips can be correlated to the neurophysiological signals acquired to give a better insight into the working of the electrode. In particular, the neurons below the electrode tips are of greater interest as these neurons are less affected by the physical penetration and chronic presence of the electrodes, and thus, yielding longer lasting recording stability. It has been argued that this may be the reason for why tip-based microelectrodes perform better than a multi-site device which has active sites along the length. Challenge has been that the neurons below the electrode tips are virtually impossible to track as fiducials following immunostaining disappear in 2D space. However, once a 3D volume is reconstructed as done in this study, it is now possible to quantify those (potentially healthier) neurons under the tips.

CHAPTER 5

CONCLUSIONS

In this study, we were able to reconstruct a true 3D image volume of the intracortical brain region of the right brain cortex of an adult male cat and carry out quantifications of important cellular entities that factor into the performance of a recording type electrode. We were able to overcome the limitations of 2D histological analysis by quantifying neurons and astrocytes below the tip of the electrode over increasing distance-bins. In addition, we were able to align whole uncropped serial tissue sections which had been a major challenge in the reconstruction of a 3D image volume which amounts to gigabytes of data. In the future, we aim to apply some additional improvements to the 3D reconstruction workflow to obtain a seamless three-dimensional tissue volume that will be an accurate representation of the hybrid microelectrode array in the intracortical tissue block.

REFERENCES

Anderson, J. R., Jones, B. W., Yang, J. H., Shaw, M. V., Watt, C. B., Koshevoy, P., … Marc, R. E. (2009). A computational framework for ultrastructural mapping of neural circuitry. *PLoS Biology*, *7*(3), 0493–0512. https://doi.org/10.1371/journal.pbio.1000074

Arganda-Carreras, I., Fernández-González, R., Muñoz-Barrutia, A., & Ortiz-De-Solorzano, C. (2010). 3D reconstruction of histological sections: Application to mammary gland tissue. *Microscopy Research and Technique*, *73*(11), 1019–1029. https://doi.org/10.1002/jemt.20829

Azaripour, A., Lagerweij, T., Scharfbillig, C., Jadczak, A. E., Willershausen, B., & Van Noorden, C. J. F. (2016). A survey of clearing techniques for 3D imaging of tissues with special reference to connective tissue. *Progress in Histochemistry and Cytochemistry*. https://doi.org/10.1016/j.proghi.2016.04.001

Berlanga, M. L., Phan, S., Bushong, E. A., Wu, S., Kwon, O., Phung, B. S., … Ellisman, M. H. (2011). Three-Dimensional Reconstruction of Serial Mouse Brain Sections: Solution for Flattening High-Resolution Large-Scale Mosaics. *Frontiers in Neuroanatomy*, *5*. https://doi.org/10.3389/fnana.2011.00017

Collinger, J. L., Wodlinger, B., Downey, J. E., Wang, W., Tyler-Kabara, E. C., Weber, D. J., … Schwartz, A. B. (2013). High-performance neuroprosthetic control by an individual with tetraplegia. *The Lancet*, *381*(9866), 557–564. https://doi.org/10.1016/S0140-6736(12)61816-9

Downey, J. E., Weiss, J. M., Muelling, K., Venkatraman, A., Valois, J. S., Hebert, M., … Collinger, J. L. (2016). Blending of brain-machine interface and vision-guided autonomous robotics improves neuroprosthetic arm performance during grasping. *Journal of NeuroEngineering and Rehabilitation*, *13*(1). https://doi.org/10.1186/s12984-016-0134-9

Duong, H., & Han, M. (2013). A multispectral LED array for the reduction of background autofluorescence in brain tissue. *Journal of Neuroscience Methods*, *220*(1), 46–54. https://doi.org/10.1016/j.jneumeth.2013.08.018

Fang, J. Y., & Tolleson, C. (2017). The role of deep brain stimulation in parkinson's disease: An overview and update on new developments. *Neuropsychiatric Disease and Treatment*. https://doi.org/10.2147/NDT.S113998

Freire, M. A. M., Morya, E., Faber, J., Santos, J. R., Guimaraes, J. S., Lemos, N. A. M., … Nicolelis, M. A. L. (2011). Comprehensive analysis of tissue preservation and recording quality from chronic multielectrode implants. *PLoS ONE*, *6*(11). https://doi.org/10.1371/journal.pone.0027554

Gilletti, A., & Muthuswamy, J. (2006). Brain micromotion around implants in the rodent somatosensory cortex. *Journal of Neural Engineering*, *3*(3), 189–195. https://doi.org/10.1088/1741-2560/3/3/001

Han, M., Manoonkitiwongsa, P. S., Wang, C. X., & McCreery, D. B. (2012). In vivo validation of custom-designed silicon-based microelectrode arrays for long-term neural recording and stimulation. *IEEE Transactions on Biomedical Engineering*, *59*(2), 346–354. https://doi.org/10.1109/TBME.2011.2172440

Hanslovsky, P., Bogovic, J. A., & Saalfeld, S. (2017). Wang, C.-W., Ka, S.-M., & Chen, A. (2014). Robust image registration of biological microscopic images. Scientific Reports, 4, 6050. https://doi.org/10.1038/srep06050Image-based correction of continuous and discontinuous non-planar axial distortion in Seri. *Bioinformatics*, *33*(9), 1379–1386. https://doi.org/10.1093/bioinformatics/btw794

Holtzheimer, P. E., & Mayberg, H. S. (2011). Deep Brain Stimulation for Psychiatric Disorders. *Annual Review of Neuroscience*, *34*(1), 289–307. https://doi.org/10.1146/annurev-neuro-061010-113638

Jimson, S., Malathi, L., Kailash Kumar, G. M., & Balachander, N. (2016). Artifact in histological section. *Biomedical and Pharmacology Journal*, *9*(2), 843–845. https://doi.org/10.13005/bpj/1014

Karumbaiah, L., Saxena, T., Carlson, D., Patil, K., Patkar, R., Gaupp, E. A., … Bellamkonda, R. V. (2013). Relationship between intracortical electrode design and chronic recording function. *Biomaterials*, *34*(33), 8061–8074. https://doi.org/10.1016/j.biomaterials.2013.07.016

Kook, G., Lee, S. W., Lee, H. C., Cho, I. J., & Lee, H. J. (2016). Neural probes for chronic applications. *Micromachines*. https://doi.org/10.3390/mi7100179

LaTorre, A., Alonso-Nanclares, L., Muelas, S., Peña, J.-M., & DeFelipe, J. (2013). 3D segmentations of neuronal nuclei from confocal microscope image stacks. *Frontiers in Neuroanatomy*, *7*. https://doi.org/10.3389/fnana.2013.00049

Liddelow, S. A., Guttenplan, K. A., Clarke, L. E., Bennett, F. C., Bohlen, C. J., Schirmer, L., … Barres, B. A. (2017). Neurotoxic reactive astrocytes are induced by activated

microglia. *Nature*, *541*(7638), 481–487. https://doi.org/10.1038/nature21029

Liu, X., McCreery, D. B., Carter, R. R., Bullara, L. A., Yuen, T. G. H., & Agnew, W. F. (1999). Stability of the interface between neural tissue and chronically implanted intracortical microelectrodes. *IEEE Transactions on Rehabilitation Engineering*, *7*(3), 315–326. https://doi.org/10.1109/86.788468

Luzzati, F., Fasolo, A., & Peretto, P. (2011). Combining confocal laser scanning microscopy with serial section reconstruction in the study of adult neurogenesis. *Frontiers in Neuroscience*, (MAY). https://doi.org/10.3389/fnins.2011.00070

Markovitz, C. D., Tang, T. T., Edge, D. P., & Lim, H. H. (2012). Three-dimensional brain reconstruction of in vivo electrode tracks for neuroscience and neural prosthetic applications. *Frontiers in Neural Circuits*, *6*. https://doi.org/10.3389/fncir.2012.00039

McCreery, D., Cogan, S., Kane, S., & Pikov, V. (2016). Correlations between histology and neuronal activity recorded by microelectrodes implanted chronically in the cerebral cortex. *Journal of Neural Engineering*, *13*(3). https://doi.org/10.1088/1741-2560/13/3/036012

Nelson, T. S., Suhr, C. L., Lai, A., Halliday, A. J., Freestone, D. R., McLean, K. J., … Cook, M. J. (2010). Seizure severity and duration in the cortical stimulation model of experimental epilepsy in rats: A longitudinal study. *Epilepsy Research*, *89*(2–3), 261–270. https://doi.org/10.1016/j.eplepsyres.2010.01.010

Nolta, N. F., Christensen, M. B., Crane, P. D., Skousen, J. L., & Tresco, P. A. (2015). BBB leakage, astrogliosis, and tissue loss correlate with silicon microelectrode

array recording performance. *Biomaterials*, *53*, 753–762. https://doi.org/10.1016/j.biomaterials.2015.02.081

Peng, H., Ruan, Z., Long, F., Simpson, J. H., & Myers, E. W. (2010). V3D enables real-time 3D visualization and quantitative analysis of large-scale biological image data sets. *Nature Biotechnology*, *28*(4), 348–353. https://doi.org/10.1038/nbt.1612

Richardson, D. S. S., & Lichtman, J. W. W. (2015). Clarifying Tissue Clearing. *Cell*, *162*(2), 246–257. https://doi.org/10.1016/j.cell.2015.06.067

Salatino, J. W., Ludwig, K. A., Kozai, T. D. Y., & Purcell, E. K. (2017). Publisher Correction: Glial responses to implanted electrodes in the brain. *Nature Biomedical Engineering*, p. 1. https://doi.org/10.1038/s41551-017-0177-7

Vigouroux, R. J., Belle, M., & Chédotal, A. (2017). Neuroscience in the third dimension: Shedding new light on the brain with tissue clearing. *Molecular Brain*. https://doi.org/10.1186/s13041-017-0314-y

Waldert, S. (2016). Invasive vs. non-invasive neuronal signals for brain-machine interfaces: Will one prevail? *Frontiers in Neuroscience*. https://doi.org/10.3389/fnins.2016.00295

Wang, C.-W., Ka, S.-M., & Chen, A. (2014). Robust image registration of biological microscopic images. *Scientific Reports*, *4*, 6050. https://doi.org/10.1038/srep06050

Weltman, A., Yoo, J., & Meng, E. (2016). Flexible, penetrating brain probes enabled by advances in polymer microfabrication. *Micromachines*. https://doi.org/10.3390/mi7100180

Yawn, R., Hunter, J. B., Sweeney, A. D., & Bennett, M. L. (2015). Cochlear implantation: a biomechanical prosthesis for hearing loss. *F1000Prime Reports*, *7*. https://doi.org/10.12703/P7-45

Yayon, N., Dudai, A., Vrieler, N., Amsalem, O., London, M., & Soreq, H. (2018). Intensify3D: Normalizing signal intensity in large heterogenic image stacks. *Scientific Reports*, *8*(1). https://doi.org/10.1038/s41598-018-22489-1